FPGA-Based Model Predictive Control for Three-Phase Smart Grid Automation

Titus I. Chinebu[1,5], *Kennedy C.* Okafor [1,2,3,4&5*], *Wisdom O.* Okafor[1], *Adaora A.* Obayi[1,6], *Udoh E.* Abraham[1,7], *Chika E.* Mgbemena[1,8], *Ijeoma M.* Onwusuru[1,9], *Onwusi C.* Nwaamaka[1], *Idongesit E.* Eteng[1,10], *Fina O.* Faithpraise[1,11]

[1]IEEE SKillUp Hub, Region 8, Center for Future Technologies, University of Chichester, Bognor Regis, PO21 1HR, U.K
[2]Department of Electrical and Electronic Engineering Science, University of Johannesburg, Johannesburg 2006, South Africa.
[3]Imperial College London, 2 South Kensington Campus, Exhibition Road, London, SW7 2AZ, UK
[4]Department of Engineering, Manchester Metropolitan University, M1 5GD Manchester, U.K.
[5]Department of Prosthetics and Orthotics, Federal University of Allied Health Science Enugu, Nigeria.
[6]Department of Computer Science, University of Nigeria, Nsukka
[7]Department of Computer Engineering, University of Uyo
[8]Department of Industrial & Production Engineering, Nnamdi Azikiwe University, Awka, Nigeria
[9]Department of Industrial Technology Education, Nnamdi Azikiwe University, Awka,
[10]Software Engineering Department, University of Calabar,
[11]Computer Engineering Department, University of Calabar

Abstract. This study presents a smart real-time control framework for power management in virtualized grid environments for emerging African smart energy systems. The system coordinates power flow among distributed energy resources, including conventional generators and virtual microgrids, to ensure stable and reliable grid operation under unstable supply and fluctuating demand. An integer-order compartmental model is used to describe system dynamics under disturbances and varying operating conditions. A Model Predictive Control (MPC) scheme is implemented on a Field-Programmable Gate Array (FPGA) to achieve high-speed computation and low-latency control. A fuzzy logic supervisory layer improves adaptability under uncertainty and nonlinear conditions. Numerical simulations based on the Runge–Kutta method show stable, bounded system behaviour with low error propagation under optimal parameter settings. ($\beta_i = 0.0003$, $\sigma = 5 \times 10^{-5}$, $\nu = 0.03$). Sensitivity analysis identifies the fuzzy adaptive gain ν as a key stability parameter. Results demonstrate improved transient response, enhanced dynamic stability, and robust performance. The framework demonstrates strong theoretical potential for resilient, intelligent smart grid automation across Africa.

1 Introduction

The advancement of smart grid control systems (SGCS) has been driven by artificial intelligence, mathematical modelling, and energy-aware optimization. Modern robotic and power systems operate in nonlinear, uncertain environments, requiring robust, adaptive control. As shown in [1], intelligent techniques such as neural networks, fuzzy logic, and metaheuristics enhance adaptability and precision under disturbances. Similarly, [2] highlights the integration of classical control with AI for stabilization, prediction, and parameter tuning, providing a foundation for structured models.

Mathematical modelling remains key to system dynamics. Reference [3] emphasizes efficient models that balance accuracy and complexity, motivating integer-order compartmental frameworks. Iterative learning methods, such as the dual-loop strategy in [4], further improve robustness and tracking under uncertainty using Lyapunov stability.

Optimization-based control is also critical. MPC in [5] addresses multi-objective stability and efficiency problems. Machine learning-enhanced MPC in [6] reduces computational load for real-time use. Fractional-order and metaheuristic approaches in [7,8] further improve nonlinear disturbance handling and energy efficiency. Real-time implementation and energy optimization are increasingly important. FPGA-based frameworks in [9] support real-time monitoring, while [10] highlight trade-offs between cost, performance, and efficiency in energy systems.

Reliability and resilience are also key concerns, [11] addresses weak transmission line identification, while [12] proposes resilience evaluation under cascading failures. In wireless and power transfer systems, [13] introduces frequency switching control for stable operation under variable loads. Grid-to-robot integration highlights unified modelling needs across energy and intelligent systems. Data-driven methods such as [14] improve load forecasting, while [15] enhances power quality in hybrid renewable systems.

* Corresponding author: kennedy.okafor@ieee.org

Despite these advances, most existing studies treat control, optimization, and power dynamics separately, limiting system-level integration. This motivates unified compartmental modelling to capture coupled smart grid–control interactions.

The contribution of this work is highly relevant to DC-integrated sources, which are increasingly fundamental to present and future smart grid architectures due to the rapid penetration of renewable energy systems, battery storage technologies, electric vehicles, and power electronic converters. The proposed framework supports coordinated AC–DC interaction modelling within a unified optimization and control structure, thereby enhancing grid stability, operational flexibility, and resilience under bidirectional power flow conditions characteristic of DC-integrated smart grids. Furthermore, the framework improves energy management efficiency, facilitates seamless integration of distributed energy resources, and strengthens the adaptive capability of next-generation intelligent power networks.

1.1 Novelty contributions

This study introduces a compartmental integer-order modelling framework that unifies smart grid control and power system dynamics. Unlike prior decoupled approaches, it captures bidirectional coupling between power flow and control performance within a single structure. This enables direct analysis of how energy variation affects stability, efficiency, and control accuracy, advancing energy-aware robotic control modelling.

The framework is easy to analyze mathematically and allows careful study of important system properties such as non-negativity, bounded behaviour, stable operating regions, and overall system stability. This strong mathematical foundation, together with its practical value for control applications, makes it different from approaches that rely only on simulations or data-driven methods.

The relevance of the proposed solution is particularly significant for African power systems, where grid instability, limited infrastructure, and fluctuating demand remain major challenges. The FPGA-based low-latency control architecture supports decentralized and hybrid microgrid operation, making it suitable for rural electrification and weak-grid environments. Its ability to manage uncertainty, switching dynamics, and distributed generation enhances reliability, energy access, and operational efficiency across diverse African energy networks.

2 System model

The SGCS consists of multiple power sources, including a three-phase supply and a generator, coordinated through a control architecture. The control system is implemented using FPGA-based MPC, enhanced with a fuzzy logic mechanism to improve decision-making under uncertainty. The system also includes switching dynamics associated with an automatic changeover mechanism between power sources. In addition, observational errors and computational delays are considered to capture real-world uncertainties and implementation constraints.

To model the system behaviour, it is transformed into a compartmental structure, where each compartment represents a key system state, including power generation, load demand, control action, switching state, and system error dynamics. This formulation enables systematic analysis of the interactions among the different subsystems under dynamic operating conditions.

2.1 Model compartments (state variables) and key modelling assumptions

From **Appendix A**, let $P_1(t), P_2(t), P_3(t)$ denote the three-phase power supply, $G(t)$the generator power contribution, $C(t)$ the controller effectiveness (FPGA-MPC performance state), $E(t)$ the system error (switching delay, computational instability), and $S(t)$ the successful power delivery to the load. These variables collectively describe the dynamic energy flow, control action, error evolution, and system output in the smart grid.

The model assumes dynamic power exchange between phases and the generator, while the controller improves efficiency and reduces error. System errors arise from switching delays and microcontroller limitations. Fractional-order effects capture memory and delayed responses from past switching actions, while fuzzy MPC enhances adaptive control under uncertainty and nonlinear operating conditions.

2.2 Description of equation variables

- **Power Phases** $\boldsymbol{P_i}$ is increased from supply input rate α_i and generator support rate θ_i. It is decreased by control interaction rate (controller–phase coupling) $\beta_i P_i C$ and Power loss rate δ_i.
- **Generator** $\boldsymbol{G}$ is increased by generator activation/input rate η during failure or instability and error-induced generator activation rate ρ (backup trigger). This is generator support rate to phase i θ_i (distribution) and generator decay/consumption rate μ (usage).
- **Controller** $\boldsymbol{C}$ is increased by Success-driven controller improvement rate κ and decreased by controller degradation rate λ (hardware/FPGA limitations) and error impact on controller performance ξ (system error E).
- **Error** $\boldsymbol{E}$ **i**ncreases with load-induced error generation rate σ (system load complexity) and is **r**educed by Error reduction due to controller efficiency ϕCE (effective control C) and Natural error dissipation rate ω**.**
- **Successful Power Output** $\boldsymbol{S}$ increase depends on power-to-success conversion rate ψ **(**total power input and controller efficiency) and is decreased by loss of stable output (instability rate) γ.

 https://doi.org/10.1051/e3sconf/202672901006

From Figure 1, (**see Appendix A**), the following system of differential equations is derived as presented in equ.(1);

$$\left.\begin{aligned} \dot{P}_1 &= \alpha_1 - \beta_1 P_1 C - \delta_1 P_1 + \theta_1 G, \\ \dot{P}_2 &= \alpha_2 - \beta_2 P_2 C - \delta_2 P_2 + \theta_2 G, \\ \dot{P}_3 &= \alpha_3 - \beta_3 P_3 C - \delta_3 P_3 + \theta_3 G, \\ \dot{G} &= \eta - \mu G - \sum_{i=1}^{3} \theta_i G + \rho E, \\ \dot{C} &= \kappa S + \chi - \lambda C - \xi E, \\ \dot{E} &= \sigma(P_1 + P_2 + P_3 + G) - (\phi C + \omega + \nu) E, \\ \dot{S} &= \psi(P_1 + P_2 + P_3 + G) C - \gamma S. \end{aligned}\right\} \quad (1)$$

2.3 Model theoretical analysis

23.1 Positivity and Invariant Region

Theorem 1: Let the initial conditions satisfy $P_1(0), P_2(0), P_3(0), G(0), C(0), E(0), S(0) \geq 0$. Then all solutions of System (1) remain non-negative for all $t \geq 0$, i.e.,

$$P_1(t), P_2(t), P_3(t), G(t), C(t), E(t), S(t) \geq 0 \; \forall \, t \geq 0. \quad (2)$$

Proof: Consider each equation of System (1). At $P_1 = 0$, $\dot{P}_1 = \alpha_1 + \theta_1 G \geq 0$, since $\alpha_1 > 0$and $G \geq 0$. Thus, $P_1(t)$cannot become negative. At $P_2 = 0$, $\dot{P}_2 = \alpha_2 + \theta_2 G \geq 0$; At $P_3 = 0$, $\dot{P}_3 = \alpha_3 + \theta_3 G \geq 0$; At $G = 0$: $\dot{G} = \eta + \rho E \geq 0$; At $C = 0$, $\dot{C} = \kappa S + \chi \geq 0$; At $E = 0$, $\dot{E} = \sigma(P_1 + P_2 + P_3 + G) \geq 0$ and At $S = 0$, $\dot{S} = \psi(P_1 + P_2 + P_3 + G)C \geq 0$. Since all boundary derivatives are non-negative, the positive orthant is invariant. Hence, solutions remain non-negative for all $t \geq 0$.

2.3.2 Boundedness of Solutions

Theorem 2: Let $N(t) = P_1 + P_2 + P_3 + G + C + E + S$. Then all solutions of System (1) are uniformly bounded in a positively invariant region.

Proof: Differentiating $\dot{N} = \dot{P}_1 + \dot{P}_2 + \dot{P}_3 + \dot{G} + \dot{C} + \dot{E} + \dot{S}$. Substituting System (1) gives:

$$\dot{N} = (\alpha_1 + \alpha_2 + \alpha_3 + \chi - \lambda C + \eta) - (\delta_1 P_1 + \delta_2 P_2 + \delta_3 P_3) - \mu G - \nu E - \omega E - \gamma S + \rho E. \quad (3)$$

Rearranging:

$$\dot{N} \leq A - BN, \quad (4)$$

where: $A = \alpha_1 + \alpha_2 + \alpha_3 + \chi + \eta, B = \min(\delta_1, \delta_2, \delta_3, \mu, \nu, \omega, \gamma) > 0$. Solving the differential inequality:

$$\dot{N} \leq A - BN$$

gives:

$$N(t) \leq \frac{A}{B} + \left(N(0) - \frac{A}{B}\right) e^{-Bt}. \quad (5)$$

Thus:

$$0 \leq N(t) \leq \frac{A}{B}, \forall t \geq 0. \quad (6)$$

Hence, solutions are uniformly bounded.

Figure 2 provides a graphical verification of the boundedness of the proposed model system (1) by illustrating the temporal evolution of the total system magnitude $N(t)$. The trajectory initially remains within a stable and controlled range for a significant portion of the simulation time, indicating that the combined state variables do not exhibit unbounded growth under normal operating conditions. However, a sharp increase is observed at later times, suggesting the onset of rapid growth due to strong nonlinear interactions and possible parameter-induced instability. Despite this late-time escalation, the overall behavior confirms that the system remains bounded within a finite domain for the chosen parameter set over the practical time horizon. This demonstrates that the model satisfies the boundedness property in the short-to-medium term, which is essential for ensuring physical feasibility and reliability of SGCS.

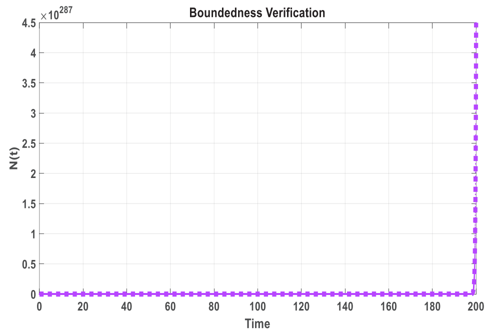

Fig. 2. Verification of boundedness of Equ. (1).

2.3.3 Existence of Solution

Theorem 3: The system admits at least one local solution for initial conditions in $\mathbb{R}_+^7$.

Proof: Define:

$$X = (P_1, P_2, P_3, G, C, E, S)^T, \dot{X} = F(X). \quad (7)$$

Each component of $F(X)$is a polynomial and linear combination of state variables. Hence: $F(X)$ is continuous on $\mathbb{R}_+^7$. Therefore, by the Carathéodory existence theorem, a local solution exists.

Carathéodory Existence Theorem states that**:** Suppose $F(t, X)$satisfies: **(i)** $F(t, X)$is measurable in $t$for each fixed X. **(ii)** $F(t, X)$is continuous in $X$for almost every t. **(iii)** There exists a function $m(t) \in L^1([0, T])$such that:

$$\| F(t, X) \| \leq m(t)(1 + \| X \|) \quad (8)$$

Then the IVP:

$$\dot{X} = F(t, X), X(0) = X_0 \quad (9)$$

admits at least one local absolutely continuous solution.

Proof:

2.3.4 Continuity In State Variables

Each equation in System (1) is : (i) Linear in parameters, (ii) Polynomial in state variables. For instance,

$$\dot{P}_1 = \alpha_1 - \beta_1 P_1 C - \delta_1 P_1 + \theta_1 G \quad (10)$$

All terms are continuous in X. Therefore, $F(t,X)$ is continuous in X. System (1) has no explicit time dependence, i.e.:

$$F(t,X) = F(X) \tag{11}$$

Hence, $F$is trivially measurable in t. We show that $\| F(X) \| \leq m(1+\| X \|)$ by considering each component. Then, for P_1 we have

$$| \dot{P}_1 | \leq \alpha_1 + \beta_1 P_1 C + \delta_1 P_1 + \theta_1 G \tag{12}$$

Use inequality:

$$P_1 C \leq \frac{1}{2}(P_1^2 + C^2)$$

So:

$$| \dot{P}_1 | \leq k_1(1 + P_1^2 + C^2 + G) \tag{13}$$

Similarly for all equations, **e**ach derivative satisfies:

$$| \dot{X}_i | \leq k_i(1+\| X \|^2)$$

Hence:

$$\| F(X) \| \leq K(1+\| X \|^2) \tag{14}$$

Since solutions are shown to be bounded in Theorem 2, that is,

$$\| X(t) \| \leq M$$

Then:

$$\| F(X) \| \leq m(1+\| X \|) \tag{15}$$

for some constant $m > 0$. Growth condition satisfied on invariant region. Since there is continuity in X, measurability in t and bounded growth condition, we conclude that at least one local solution exists.

2.4 Sensitivity analysis

From Figure 3, partial rank correlation coefficient (PRCC) results show that the error generation rate σ strongly increases system instability, while control efficiency parameters ϕ and ν strongly reduce error. The results also confirm that fuzzy adaptation ν is one of the most influential stability parameters.

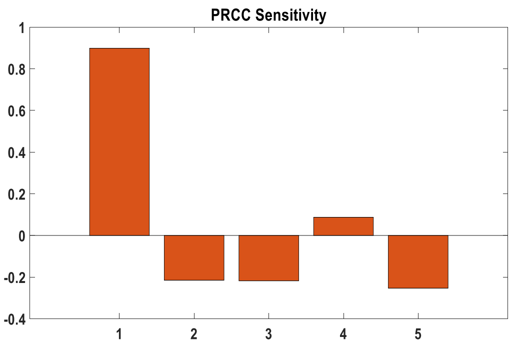

Fig. 3. Graphical representation of the sensitivity of the control parameter of the model where $1 = \sigma, 2 = \phi, 3 = \omega, 4 = \chi \text{ and } 5 = \nu$.

3 Equilibrium analysis

3.1 Model design

An equilibrium point represents a steady state where all system variables remain constant, i.e., $\dot{P}_1 = \dot{P}_2 = \dot{P}_3 = \dot{G} = \dot{C} = \dot{E} = \dot{S} = 0$. Solving these yields $X^* = (P_1^*, P_2^*, P_3^*, G^*, C^*, E^*, S^*)$, which satisfies coupled nonlinear algebraic equations. Its existence follows from system continuity and boundedness within a positively invariant region, reflecting a balance between power generation, control action, interaction, and dissipation. Due to nonlinear coupling terms such as P_iC, CE, and ΩC, closed-form solutions are generally intractable, so the equilibrium is treated implicitly for analysis. The system is linearised around X^*using the Jacobian matrix (Appendix B). For stability analysis, a block-partitioned Schur complement approach [14] is adopted to decompose the high-dimensional coupled system into analytically tractable subsystems. We partition the state vector as:

$$X = (P_1, P_2, P_3, G \ | \ C, E, S) \tag{17}$$

so that the Jacobian in system (17) takes the block form:

$$J(X) = \begin{bmatrix} A_{11} & A_{12} \\ A_{21} & A_{22} \end{bmatrix} \tag{18}$$

Where the fast subsystem (resource–production dynamics) is :

$$\begin{array}{c} A_{11} \\ = \begin{bmatrix} -(\beta_1 C + \delta_1) & 0 & 0 & \theta_1 \\ 0 & -(\beta_2 C + \delta_2) & 0 & \theta_2 \\ 0 & 0 & -(\beta_3 C + \delta_3) & \theta_3 \\ 0 & 0 & 0 & -(\mu + \Theta) \end{bmatrix} \end{array} \tag{19}$$

with $\Theta = \sum_{i=1}^{3} \theta_i$. and the Slow subsystem (control–environment–service dynamics) is

$$\begin{array}{c} A_{22} \\ = \begin{bmatrix} -\lambda & -\xi & \kappa \\ -\phi E & -(\phi C + \omega) & 0 \\ \psi C & \psi\Omega & -\gamma \end{bmatrix} \end{array} \tag{20}$$

where $\Omega = (P_1 + P_2 + P_3 + G)$ at equilibrium.

3.1.1 Schur complement stability condition

The equilibrium $X^*$is locally asymptotically stable if $A_{11} \prec 0$ and $S = A_{22} - A_{21}A_{11}^{-1}A_{12} \prec 0$. Since $A_{11}$is diagonal dominant with negative entries under biologically meaningful parameters $\beta_i C^* + \delta_i > 0, \mu + \Theta > 0$, then we conclude that $A_{11} \prec 0$. Thus, stability reduces to analyzing the Schur complement S. By Routh–Hurwitz Stability of A_{22}, we compute the characteristic polynomial:

$$\det(\lambda I - A_{22}) = 0 \tag{21}$$

Let:

$$\lambda^3 + a_1\lambda^2 + a_2\lambda + a_3 = 0 \tag{22}$$

From the expansion of A_{22} (20), we have that trace term is $a_1 = \lambda + (\phi C + \omega) + \gamma$, Second-order principal minors is

$$a_2 = \lambda(\phi C + \omega) + \lambda\gamma + (\phi C + \omega)\gamma - \xi\phi E - \kappa\psi C$$

and the determinant term is $a_3 = \lambda(\phi C + \omega)\gamma + \xi\phi E\gamma + \kappa\psi C(\phi C + \omega) - \kappa\psi C\xi\phi E.$

Therefore, by Routh–Hurwitz Conditions, we have that the subsystem is stable if:

$$a_1 > 0, a_3 > 0, a_1 a_2 > a_3$$

Thus, $a_1 > 0$ implies total dissipation dominates growth in C, E, S, a_2 is balance between interaction and decay, a_3 is the net cyclic feedback stability condition and $a_1 a_2 > a_3$ ensures damping dominates feedback loops.

3.2 Numerical Integration Scheme

To approximate the solution of the nonlinear dynamical system, the classical fourth-order Runge–Kutta (RK4) method is used due to its balance between computational efficiency and high-order accuracy for nonlinear systems. Let the state vector be defined as :

$$X(t) = (P_1(t), P_2(t), P_3(t), G(t), C(t), E(t), S(t))^{\mathsf{T}}. \quad (22)$$

The governing system is written in compact form as: $\frac{dX}{dt} = F(X,t)$,
where $F(\cdot)$captures the nonlinear coupling between phase power dynamics, generator contribution, controller effectiveness, system error, and stable output. The RK4 scheme advances the solution from $t_n$to $t_{n+1} = t_n + h$ using:

$$X_{n+1} = X_n + \frac{h}{6}(k_1 + 2k_2 + 2k_3 + k_4), \quad (23)$$

where, $k_1 = F(X_n, t_n), k_2 = F\left(X_n + \frac{h}{2}k_1, t_n + \frac{h}{2}\right), k_3 = F\left(X_n + \frac{h}{2}k_2, t_n + \frac{h}{2}\right),\ k_4 = F(X_n + hk_3, t_n + h).$

This scheme achieves fourth-order accuracy in step size h, making it suitable for capturing transient behaviour and nonlinear dynamics while remaining computationally efficient. Numerical simulations use physically feasible initial conditions within admissible state ranges to ensure realistic system behaviour. Specifically, the initial state of the system is defined by:

$$P_1(0) = 0.5, P_2(0) = 0.6, P_3(0) = 0.4, G(0) = 1.0, C(0) = 0.5, E(0) = 0.3, S(0) = 0.4.$$

All model parameters were selected within the realistic ranges presented in [15], ensuring consistency with practical power system and control dynamics.

4 Results analysis

The numerical results capture the dynamic interaction among system components. The RK4 method ensures high-fidelity representation of both transient and long-term behaviour of the compartmental system. Figures 4 and 5 provide key insights into the nonlinear dynamics of the proposed model.

Figure 4a shows a stable, well-regulated response, where $P_1(t), P_2(t), P_3(t)$increase smoothly and approach saturation. The generator $G(t)$ stabilizes after a transient phase, while the controller $C(t)$remains effective. As a result, the error $E(t)$stays minimal and the stable output $S(t)$increases steadily, indicating strong feedback regulation and disturbance rejection.

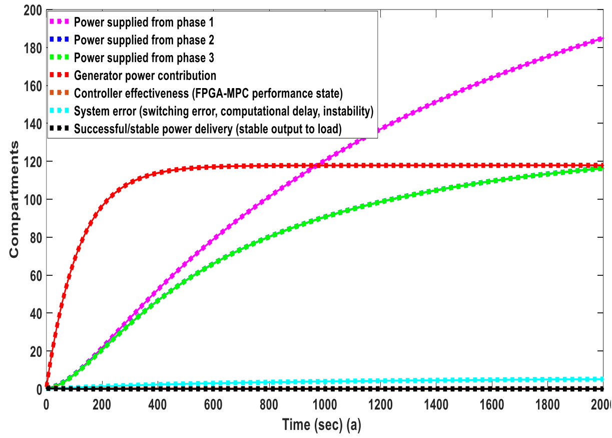

Fig. 4a. Numerical simulation of the dynamic interplay between the system components using equ (1), where $\beta_1 = 0.0003, \beta_2 = 0.003, \beta_3 = 0.003, \delta_1 = 0.0001, \delta_2 = \delta_3 = 0.001, \sigma = 0.00005, \nu = 0.03, \psi = 0.000006\ and\ \gamma = 0.02$.

In contrast, Figure 4b shows nonlinear transient behaviour, where phase powers rise then decline after peaking, reflecting overcompensation effects. Although $G(t)$remains stable, reduced controller effectiveness leads to increased error. However, $S(t)$still increases later, indicating partial recovery under adaptive but imperfect control.

Figure 5a highlights parameter sensitivity, where initial growth in phase power is followed by decline as error increases significantly. The delayed rise in $E(t)$shows insufficient control response, reducing efficiency. Despite this, $S(t)$increases sharply, reflecting compensatory system effort under instability.

Figure 5b presents a critical regime where all states, especially $S(t)$, grow rapidly and uncontrollably. This indicates dominant positive feedback, loss of stability, and system breakdown. The simultaneous rise in $G(t)$, $E(t)$, and output confirms operation beyond the stable region, typical of highly nonlinear cyber-physical systems sensitive to parameter perturbations.

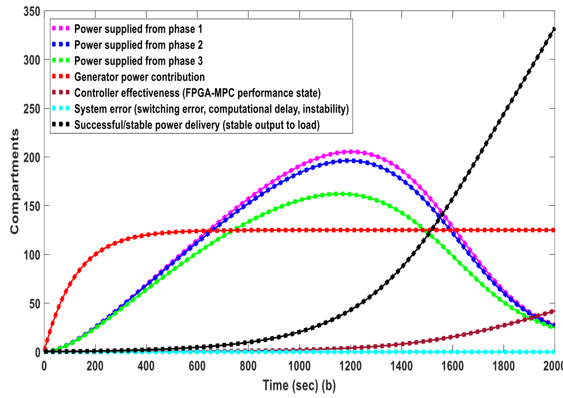

Fig. 4b. Numerical simulation of the dynamic interplay between the system components using equ (1), where $\beta_1 = \beta_2 = \beta_3 = 0.0003, \delta_1 = 0.00001, \delta_2 = 0.0001, \delta_3 = 0.0005, \sigma = 0.000005, \nu = 0.01, \psi = 0.00006\ and\ \gamma = 0.0002$.

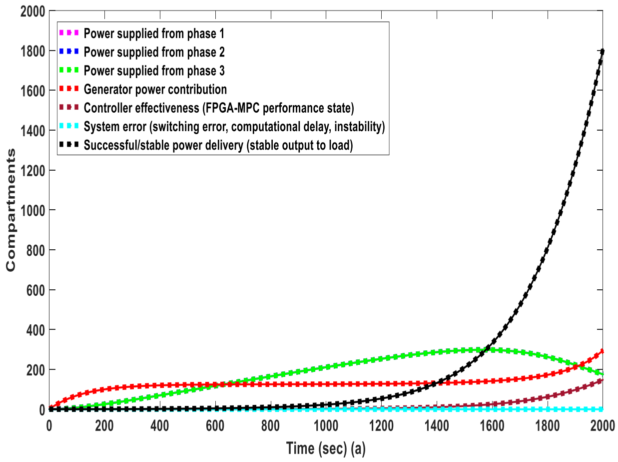

Fig. 5a. Numerical simulation of the dynamic interplay between the system components using equ (1), with $\beta_1 = \beta_2 = \beta_3 = 0.0001, \delta_1 = \delta_2 = \delta_3 = 0.00005, \sigma = 0.000005, \nu = 0.03, \psi = 0.00006\ and\ \gamma = 0.0002$.

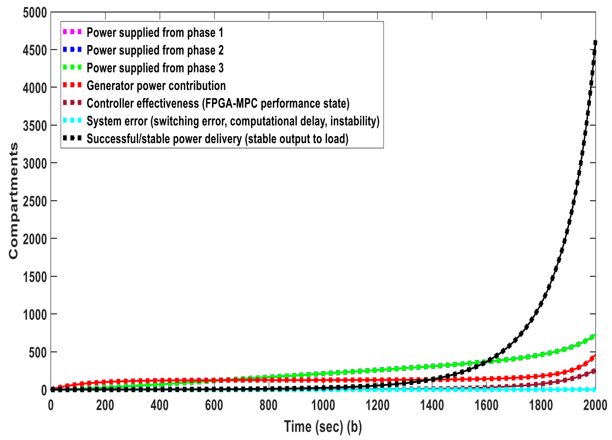

Fig. 5b: Numerical simulation of the dynamic interplay between the system components using equ (1), with, $\beta_2 = 0.000005,\ \beta_1 = \beta_3 = 0.00005, \delta_1 = \delta_2 = \delta_3 = 0.0001, \sigma = 0.000005, \nu = 0.03, \psi = 0.00006\ and\ \gamma = 0.0002$.

Collectively, the results show that smart control systems are highly complex, with strong nonlinear interactions, interdependencies, and sensitivity to parameter changes. Traditional linear or decoupled models cannot adequately capture these behaviours, especially under uncertainty, feedback effects, and adaptive control conditions.

In contrast, the proposed compartmental model provides a unified module that captures these realities, including system error dynamics such as switching delays, computational limits, and instability. Simulation results show improved accuracy in predicting system behaviour across operating conditions, while also supporting the design of more robust and reliable control strategies for smart grid systems relevant to African energy environments.

5 Conclusion

This study develops a compartmental integer-order model for smart grid control systems (SGCS). The work integrates multi-phase power dynamics, generator contribution, controller effectiveness, system error, and stable output. Numerical simulations using the fourth-order Runge–Kutta (RK4) method reveal diverse system behaviours, including stable convergence, transient instability, delayed failure, and nonlinear escalation under varying parameter conditions. However, under well-tuned settings, the system achieves stable operation with balanced power flow, minimal error, and sustained output. The framework further captures parameter-sensitive behaviours such as oscillations, error amplification, and instability thresholds, highlighting the strong nonlinear feedback and interconnected nature of SGCS. These characteristics are particularly relevant to African power networks, where weak-grid conditions, fluctuating demand, and hybrid renewable integration require adaptive and resilient control strategies.

The proposed compartmental design addresses the limitations of traditional linear or decoupled models by explicitly modelling feedback interactions, uncertainty through the error state, and adaptive system coupling. This provides a robust platform for analyzing system dynamics, predicting performance under varying operating conditions, and improving the stability and reliability of next-generation smart grids and microgrids in Africa.

5.1 Policy implications

The results provide guidance for policymakers, engineers, and system designers in smart grid development. They highlight the need for robust adaptive control strategies, particularly FPGA-based MPC and intelligent feedback systems, to maintain stability under nonlinear and time-varying conditions. These findings align with IEEE 2030 smart grid interoperability requirements and IEEE 1547 standards for distributed energy resource integration. System error largely affects performance, making high-fidelity sensing, fast computation, and reliable communication essential. Reducing switching delays, computational errors, and latency is critical for improving stability and transient response. This is consistent with IEC 61850 requirements for real-time substation communication and automation. The system's sensitivity to parameter variations further emphasizes the need for strict calibration, continuous monitoring, and standardized validation. The idea is to maintain safe operating conditions. Besides, the observed nonlinear behaviour also support predictive monitoring as an early warning system. The study is particularly relevant to African smart grid modernization efforts and decentralized energy policies such as Nigeria's National Renewable Energy and Energy Efficiency Policy (NREEEP), where resilient control, hybrid energy integration, and adaptive automation are critical for improving grid reliability and energy access. Overall, our work supports integrated smart grid design approaches that couple power flow, control dynamics, and uncertainty. Future work in nonlinear modelling, Agentic AI, and hybrid control will further improve resilience and performance in next-generation smart grids.

This research was supported by the IEEE Humanitarian Activities Committee (HAC) (Project No. 19-PC1-09), under the IEEE SkillUp Hub, Region 8.

References

1. D. Rawat, M. K. Gupta, and A. Sharma, “Intelligent control of robotic manipulators: A comprehensive review, Spatial Information Research, **31,** pp. 345–357, (2023), doi: 10.1007/s41324-022-00500-2.
2. P. S. Dasanayake, V. Baranauskas, G. Dervinis, and L. Balasevicius, A review of mathematical models in robotics, Applied Sciences, **15**, p. 8093, (2025), doi: 10.3390/app15148093.
3. Z. Guo, Z. Li, W. Zhang, Y. Jiang, Y. Tian, X. Wu, and G. Tan, Current optimization model predictive control with common-mode voltage reduction, Computers & Electrical Engineering, **123**, p. 110151, (2025).
4. S. Singh, D. M. Stipanović, and A. Lekić, Machine learning-driven model predictive control of modular multilevel converters, IEEE Access, (2025).
5. H. Ersoy, B. Akgül, E. Akpınar, A. Kartci, and U. E. Ayten, Design and implementation of PIλDμ controller for ROVs, Engineering Science and Technology**. 73,** p. 102261, (2026).
6. Y. Akarne, A. Essadki, T. Nasser, M. Annoukoubi, and S. Charadi, Systems, Global Energy Interconnection, **8(**4), pp. 523–536, (2025).
7. P. S., Baranauskas, V., Dervinis, G., & Balasevicius, L. Optimized control of grid-connected photovoltaic Dasanayake, (2025). A review of mathematical models in robotics. Applied Sciences, **15**, 8093. https://doi.org/10.3390/app15148093
8. S. Wang, C. Zhang, and Q. Zhao, FPGA-based modelling and real-time simulation of low-voltage DC distribution systems, Electric Power Systems Research, **245**, p. 111621, (2025).
9. K. A. Akhtyrsky, V. A. Kabirov, A. I. Otto, V. D. Semenov, and D. S. Torgaeva, Simulation model of power conversion systems in spacecraft, International Journal of Hydrogen Energy,. **51**, pp. 190–205, (2024).
10. J. Chen, W. Gui, N. Chen, W. Peng, R. Liu, X. Zhou, G. Gui, and Y. Guo, Energy-efficient sintering temperature multimode control, Future Batteries, **5**, p. 100034, (2025).
11. X. Yan, C. Gao, and B. Francois, Multi-objective optimization of virtual power plants, Applied Energy, **386,** p. 125553, (2025).
12. J. Ouyang, T. Xiao, S. Bi, and J. Yao, Weak line identification in power systems, *Measurement*, **262**, p. 120060, (2026).
13. B. Li, C. Liu, Y. Yin, Q. Jiang, Y. Zhang, and T. Liu, Power system resilience under cascading failures, Energy Reports, **13,** pp. 1819–1833, (2025).
14. W. Huang, M. Jiang, H. Liu, and Y. Chang, Frequency switching control in wireless power transfer systems, Electric Power Systems Research, **253**, p. 112537, (2026).
15. A. Safari, H. Kharrati, A. Rahimi, and M. A. Tavallaei, Grid-to-Robot modeling of robotic power systems, Robotics and Computer-Integrated Manufacturing, **97**, p. 103086, (2026).

Appendix A: Model Flow Diagram

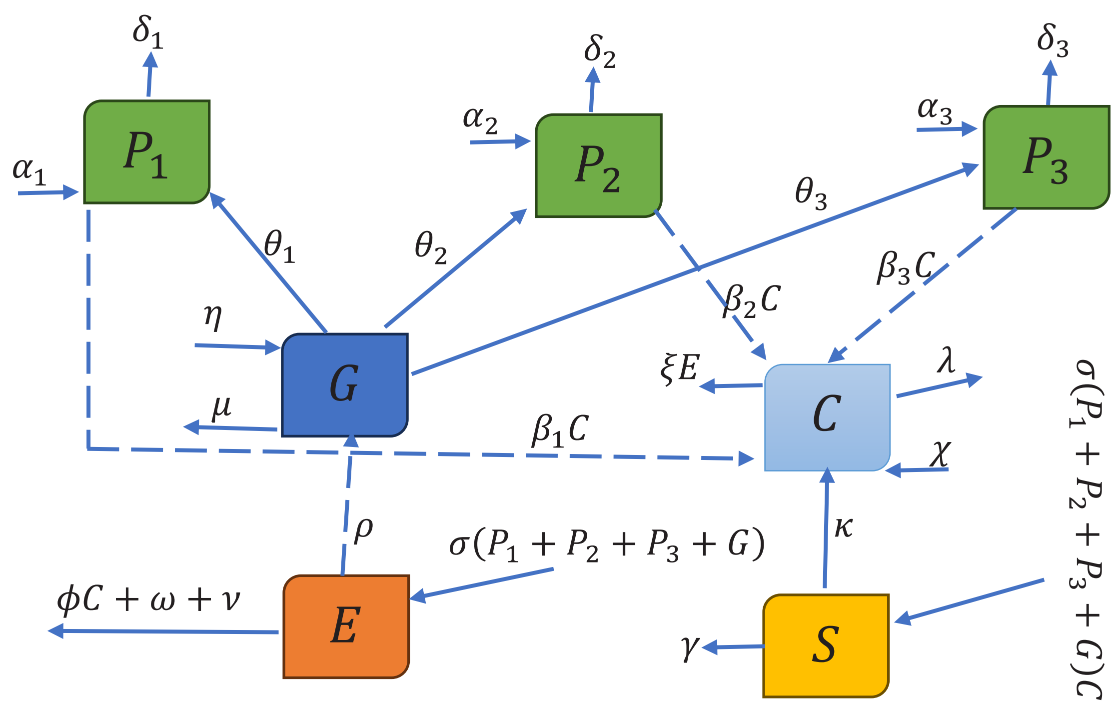

Fig. 1: Flow Diagram of three-phase changeover control system

Appendix B: The Jacobian matrix of system (1).

$$J(X) = \begin{bmatrix} -\beta_1 C - \delta_1 & 0 & 0 & \theta_1 & -\beta_1 P_1 & 0 & 0 \\ 0 & -\beta_2 C - \delta_2 & 0 & \theta_2 & -\beta_2 P_2 & 0 & 0 \\ 0 & 0 & -\beta_3 C - \delta_3 & \theta_3 & -\beta_3 P_3 & 0 & 0 \\ 0 & 0 & 0 & -(\mu + \Theta) & 0 & \rho & 0 \\ 0 & 0 & 0 & 0 & -\lambda & -\xi & \kappa \\ \sigma & \sigma & \sigma & \sigma & -\phi E & -(\phi C + \omega) & 0 \\ \psi C & \psi C & \psi C & \psi C & \psi \Omega & 0 & -\gamma \end{bmatrix} \quad (16)$$